Experimental Verification of the Formation Mechanism for Pillar Arrays in Nanofilms Subject to Large Thermal Gradients

Euan McLeod, Yu Liu, and Sandra M. Troian*

California Institute of Technology, 1200 E. California Blvd., T. J. Watson Sr. Laboratories of Applied Physics, MC 128-95, Pasadena, California 91125, USA

(Received 15 November 2010; published 25 April 2011)

The free surface of molten nanofilms is known to undergo spontaneous formation of periodic protrusions when exposed to a large transverse thermal gradient. Early time measurements of the array pitch and growth rate in polymer melts confirm a formation process based on a long wavelength thermocapillary instability and not electrostatic attraction or acoustic phonon driven growth as previously believed. We find excellent agreement with theoretical predictions provided the nanofilm out-of-plane thermal conductivity is several times larger than bulk, an enhancement suggestive of polymer chain alignment.

DOI: 10.1103/PhysRevLett.106.175501 PACS numbers: 81.16.Dn, 47.55.nb, 66.70.Hk, 68.35.bm

For the past decade, researchers have been exploring the effects of large thermal gradients on molten nanofilms in the hope of harnessing pillar instabilities for generating microarrays [1–4]. When the free surface of a molten nanofilm is exposed to large thermal gradients, periodic protrusions form and grow toward the cooler target until contact is achieved. There is significant interest in this phenomenon since external field gradients can be used to generate three dimensional nanostructures directly from the melt, which after solidification exhibit ultra smooth surfaces befitting the most demanding optical applications. Controlled growth of desired shapes, however, requires identification of the dominant growth mechanism, the material and geometric properties affecting structure formation, and the principles that establish the minimum feature size.

Three different mechanisms have been proposed as the source of instability: electrostatic attraction from surface induced charge between the film and overlying substrate (SC model [2,5]), internal film pressure caused by interfacial reflections of low frequency acoustic phonons (AP model [3,6]), and thermocapillary flow from temperature variations along the interface which draw fluid toward cooler regions (TC model [7,8]). The first two mechanisms rely on properties specific to polymeric films. The thermocapillary mechanism is applicable to any liquid nanofilm—it represents an extreme limit of (Bénard) Marangoni instability for long wavelength fluctuations in which gravitational effects are absent and thermocapillary forces overcome stabilization by capillary forces. Previous experimental investigations have confronted limitations imposed by the typical setup shown in Fig. 1(a), namely, no direct measure of the thermal gradient within the narrow gap, lack of parallelism between opposing substrates, and lack of visualization during structure formation and growth. In fact, all measurements to date have relied on solidified formations resulting from prolonged contact with the cooler target.

We find that physical contact with the overlying substrate results in smaller wavelengths from fluid reorganization. While this ultimately reduces the array pitch, it compromises direct comparison to models based on linear stability analysis, which also require amplitude fluctuations small in comparison to the initial film thickness. In this Letter, we report *in situ* optical microscopy measurements of the lateral spacing and growth time for evolving protrusions in polymer nanofilms. Excellent quantitative agreement with the thermocapillary model is

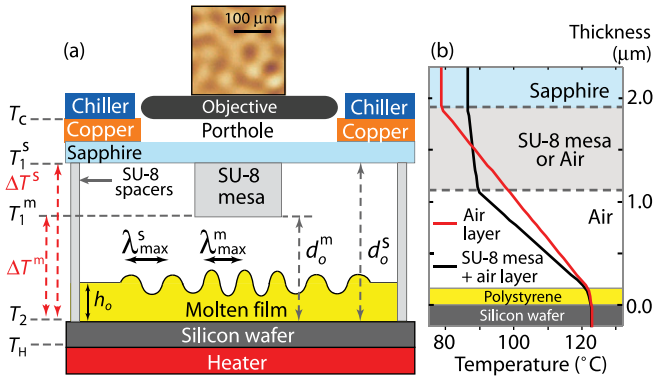

FIG. 1 (color online). (a) Experimental setup (not to scale) showing actual image of molten film deformation at early times. Fastest growing wavelength beneath sapphire (s) and mesa (m) regions are denoted by $\lambda^s_{\max}$ and $\lambda^m_{\max}$. (b) Sample temperature profiles from steady-state finite element simulations (FEM) [10] with axial symmetry, constant temperatures T_H and T_C, and insulating conditions along exterior boundaries. For $T_H = 130\,^\circ\mathrm{C}$, $T_C = 25\,^\circ\mathrm{C}$, mesa diameter $= 400\ \mu$m, $h_0 = 160$ nm, $d^m_0 = 1100$ nm and $d^s_0 = 1900$ nm, results yield $T_2 = 123\,^\circ\mathrm{C}$, $\Delta T^m = 33.2\,^\circ\mathrm{C}$ and $\Delta T^s = 44.8\,^\circ\mathrm{C}$. Black curve (mesa central axis): $T(r = 0, z)$; red curve: $T(r = 700\ \mu\mathrm{m}, z)$. Thermal conductivity constants [W/m K] used in FEM simulations: silicon $=$ 93 at 130 °C [18], copper $=$ 390 at 40 °C [19], sapphire $=$ 40 at 60 °C [20], SU 8 $=$ 0.3 (MicroChem), air $=$ 0.033 at 110 °C [19], and polystyrene (PS) $=$ 0.13 at 130 °C [11].

obtained so long as the out-of-plane film thermal conductivity is several times larger than reported bulk values, an enhancement suggestive of polymer chain alignment.

Figure 1(a) depicts a sketch of the experimental apparatus used in our experiments. The bottom substrate consisted of a polished silicon (Si) wafer (Ultrasil, ⟨100⟩, 150 mm diameter, 650–700 μm thickness, 50–60 Ω cm) cleaned with piranha solution and rinsed in 18 MΩ water (Millipore Milli-Q). A solution of polystyrene (PS) (4 wt % of $M_w = 2.46$ kg/mol, $T_g = 60\,^{\circ}$C [9] or $M_w = 1.3$ kg/mol, $T_g = 23\,^{\circ}$C [9], Scientific Polymer Products) in toluene was extracted through a 0.2 μm PTFE filter and spun coat onto the wafer. Films were vacuum baked at 80 °C for two hours to remove residual toluene; the resulting thickness h_0 of the wetting film was measured by ellipsometry (Gaertner L166C). The top substrate consisted of a cylindrical sapphire window (Edmund Optics, single crystal, diameter 7.5 mm, thickness 400 ± 50 μm) patterned with four photoresist spacers (MicroChem, SU-8 2000) of length $d_0^s = 2.0 \pm 0.1$ μm arranged at the vertices of a square measuring either 1 mm (for 2.46 kg/mol films) or 3 mm (for 1.3 kg/mol films) along the diagonal. Centered between these spacers was a transparent cylindrical SU-8 mesa of diameter 400 μm (for 2.46 kg/mol films) or 1 mm (for 1.3 kg/mol films) and thickness 0.6 to 1.4 μm. To prevent polymer adhesion, the sapphire window and protrusions were silanized after a hard-bake of the SU-8 by exposure to a solution of 10 mL of hexane with 2 drops of FOTS (CAS 78560-45-9) inside an evacuated desiccator. The PS coated wafer was then placed on top of a copper sheet (1.59 mm thick) resistively heated from below by a glass slide coated with an indium tin oxide layer. The entire system was clamped between a bottom aluminum plate and a second top copper sheet (1.59 mm thick) using three long vertical screws. The copper sheet was perforated with a small hole centered above the SU-8 mesa to view structure formation *in situ*. Perfect parallelism over an extended region was difficult to achieve due to intrinsic limitations on surface flatness (sapphire 2λ@632.8 nm) and total thickness variation (Si wafer <5 μm). To maximize parallelism, the three screws were adjusted to distribute the clamping force while monitoring the resulting interference fringes.

The bottom of the Si wafer was maintained at $T_H = 130\,^{\circ}$C (2.46 kg/mol films) or 114 °C (1.3 kg/mol films) by a temperature controller (Wavelength Electronics, MPT10000); the exterior face of the top copper sheet was maintained at $23\,^{\circ}\text{C} \le T_C \le 72\,^{\circ}$C by a chilled water loop. Both temperatures were monitored by thermocouples (Omega, J type, calibration error ±1 °C). The extremely small gap size d_0^s prevented direct measurement of the temperature difference $\Delta T^{m,s} = T_2 - T_1^{m,s}$ needed for comparison to theoretical models. Finite element simulations (FEM) [10] based on the dimensions and material properties of the elements shown in Fig. 1 were therefore used to compute $\Delta T^{m,s}$. As discussed in Ref. [8], the long wavelength (slender gap) approximation reduces the heat transfer process to a 1D thermal conduction problem along the vertical axis. Shown in Fig. 1(b) are sample temperature profiles beneath the mesa central axis ($r = 0$) and at a radial distance $r = 700$ μm. These profiles clearly indicate the difference between the value $\Delta T^{m,s}$ and the external value $T_H - T_C$.

In situ measurements of the pattern wavelengths and growth times were obtained by optical microscopy (Zeiss Axiovert 200 MAT) and white light interferometry, respectively. Images were captured from two distinct regions: that beneath the SU-8 mesa characterized by d_0^m, ΔT^m, and $\lambda_{\max}^m$, and that beneath the sapphire window (and away from the mesa, spacers and top copper sheet) characterized by d_0^s, ΔT^s, and $\lambda_{\max}^s$. Altogether, these experiments spanned a wide parameter range, namely $81\text{ nm} \le h_0 \le 204\text{ nm}$, $600\text{ nm} \le d_0 \le 2000\text{ nm}$, $3 \le d_0/h_0 \le 23.5$ and $13\,^{\circ}\text{C}/\mu\text{m} \lesssim \Delta T^{m,s}/d_0^{m,s} \lesssim 43\,^{\circ}\text{C}/\mu\text{m}$.

Figures 2(a) and 2(b) show representative images of structure formation beneath the cooled mesa at (a) early times and (b) after contact by several nanopillars. Here, the

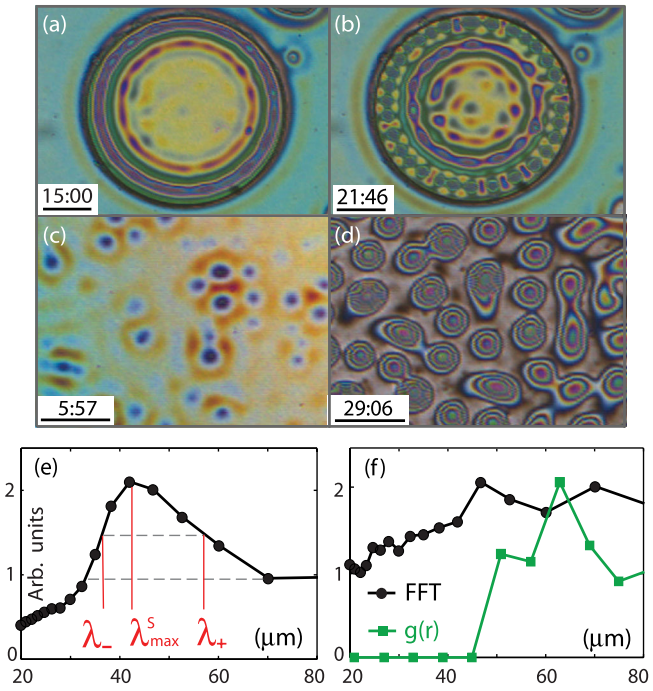

FIG. 2 (color online). Film deformation and growth beneath a 400 μm diameter mesa (a) at early times and (b) after contact for $h_0 = 160$ nm, $d_0 = 630$ nm and $\Delta T^m = 17\,^{\circ}$C. See supplemental material [15] for a movie of this process. Corresponding images in exterior region away from mesa at (c) early times and (d) late times for $h_0 = 160$ nm, $d_0 = 1900$ nm and $\Delta T^s = 45\,^{\circ}$C. Latter images show significant film depletion—pink regions in interstitial areas $\approx O(10$ nm). (e) Fourier transform of blue channel of image (c) with $\lambda_{\max}^s = 42.2$ μm and bandwidth spread (full width half-maximum) $\lambda_- = 36.8$ μm and $\lambda_+ = 56.1$ μm. (f) Comparison of pair correlation function $g(r)$ with Fourier transform (blue channel) of image (d). Time stamp = hours : minutes; scale bar = 100 μm. Color levels in (a)–(d) adjusted for enhanced contrast.

mesa perimeter triggered axisymmetric undulations in film thickness which grew to touch the colder substrate. Approximately 18 protrusions formed along the outer ridge before contact [Fig. 2(a)]; approximately 31 were observed after contact [Fig. 2(b)]. The smaller wavelength after contact resulted from rapid fluid rearrangement against the silanized (mesa) substrate. Figures 2(c) and 2(d) show corresponding images in the exterior region away from the mesa at (c) early times and (d) late times. Here, taller protrusions sometimes underwent coalescence, which resulted in larger values of $\lambda_{\max}^{s}$, or film depletion, which eventually hindered growth. All data for comparison to linear stability theory was therefore restricted to protrusions which neither touched the cooler substrate nor underwent coalescence or film depletion.

Fourier transforms of images to extract $\lambda_{\max}$ were obtained from the color channel that exhibited highest contrast. The first circular ridge to form beneath the edge of the mesa was also excluded from analysis to minimize edge effects. Measurements of $\lambda_{\max}$ versus radial distance were conducted to rule out finite size effects. Figure 2(e) is a sample Fourier transform of the blue channel for image (c). For structures containing many interference fringes, the quality of the Fourier transform was diminished, as shown in Fig. 2(f). In such cases, $\lambda_{\max}$ was instead extracted from the peak in the pair correlation function $g(r)$.

The wavelength of the fastest growing mode in the limit $(h_0/\lambda_{\max})^2 \ll 1$ for the three models discussed above [2,3,8] is given by

$$\frac{\lambda_{\max}^{\mathrm{SC}}}{2\pi h_0} = \sqrt{\frac{2\varepsilon_0\varepsilon_p^2\gamma h_0}{\sigma^2 d_0^2}}\left(\frac{d_0}{h_0}+\frac{1}{\varepsilon_p}-1\right)^{3/2}, \tag{1a}$$

$$\frac{\lambda_{\max}^{\mathrm{AP}}}{2\pi h_0} = \sqrt{\frac{\gamma u_p}{Q(1-\kappa)k_{\mathrm{air}}\Delta T}}\left(\frac{d_0}{h_0}+\kappa-1\right), \tag{1b}$$

$$\frac{\lambda_{\max}^{\mathrm{TC}}}{2\pi h_0} = \sqrt{\frac{4\gamma h_0}{3\kappa d_0\gamma_T\Delta T}}\left(\frac{d_0}{h_0}+\kappa-1\right). \tag{1c}$$

TABLE I. Literature values for material constants of molten polystyrene at $T = 130\,^{\circ}\mathrm{C}$ unless otherwise noted: H = 2.46 kg/mol and L = 1.3 kg/mol. E denotes extrapolated value.

γ	Surface tension [11] (E)	31 mN/m (H) 33 mN/m (L)
γ_T	$\lvert\partial\gamma/\partial T\rvert$ [11] (E)	0.076 mN/m K (H) 0.078 mN/m K (L)
η	Shear viscosity [9] (E)	85 Pa s (H, 125 °C) 7.8 Pa s (L, 107 °C)
ε_p	Dielectric constant [11] (M_w and T unknown)	2.5
u_p	Speed of sound [12] (M_w and T unknown)	1300 m/s
k_p	Thermal conductivity [11] (E) (M_w and T unknown)	0.13 W/m K

Here, σ denotes the polymer surface charge density, ε_0 is the vacuum permittivity, Q is the nanofilm acoustic quality factor [3], and $\kappa = k_{\mathrm{air}}/k_p$, which represents the thermal conductivity ratio of air to polymer film. Remaining variables are defined in Fig. 1 and Table I. The AP and TC models both predict that $\lambda_{\max}$ scales as $(\Delta T)^{-1/2}$; the SC model contains no temperature dependence.

Figure 3(a) shows the dependence of $\lambda_{\max}$ on ΔT i.e. ΔT^m or ΔT^s as computed from FEM simulations. Least squares fits to the power law $\lambda_{\max} \propto (\Delta T)^{\zeta}$ resulted in an average value $\zeta = -0.47$, close to the predicted value $-1/2$. The measured exponent is consistent with the AP and TC models but not the SC model. Shown in Fig. 3(b) is a least squares fit to the SC model as a function of d_0 with $\sigma = 0.24\ \mathrm{mC/m^2}$. Not only is the agreement poor but the fit constant σ is 1 to 2 orders of magnitude larger than reported in the literature [13]. These results indicate that the SC mechanism is likely not the primary cause of instability.

To differentiate between the AP and TC mechanisms, we examined the behavior of $\lambda_{\max}$ as a function of gap ratio d_0/h_0, i.e., d_0^m/h_0 or d_0^s/h_0. Superimposed on the data in Fig. 4(a) are the theoretical predictions of Eqs. (1b) and (1c). The (black) dashed line is the TC model with bulk material constants from Table I, which yields an unacceptable fit. The (orange) dashed curve is the AP model with fitting constant $Q = 2.3$ (cf. $Q = 6.2$ for PS between two Si wafers [3]). The linear increase with d_0/h_0 is not supported by the data. A two parameter fit to Eq. (1b) yielded better agreement but unphysical constants, namely $Q = -0.56$ (positive value required for low frequency phonon model [3]) and $k = 0.0026$ W/m K (value must exceed $k_{\mathrm{air}} = 0.033$ W/m K). The solid (black) curve is

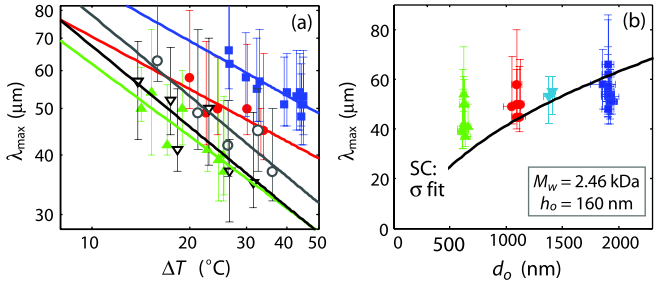

FIG. 3 (color online). (a) Least squares fit (solid lines) to power law $\lambda_{\max} \propto (\Delta T)^{\zeta}$. Error bars denote bandwidth spread λ_+ to λ_- defined in Fig. 2(e). Fits are based on $\lambda_{\max}$ values (excluding error bars). Parameter values for lines shown: solid (blue) squares: $M_w = 2.46$ kg/mol, $h_0 = 160 \pm 10$ nm, $d_0 = 1900 \pm 100$ nm, $\zeta = -0.38 \pm 0.13$; solid (red) circles: $M_w = 2.46$ kg/mol, $h_0 = 160 \pm 10$ nm, $d_0 = 1100 \pm 50$ nm, $\zeta = -0.36 \pm 0.31$; open (grey) circles: $M_w = 1.3$ kg/mol, $h_0 = 186 \pm 5$ nm, $d_0 = 873 \pm 45$ nm, $\zeta = -0.56 \pm 0.42$; open (black) triangles: $M_w = 1.3$ kg/mol, $h_0 = 186 \pm 5$ nm, $d_0 = 655 \pm 45$ nm, $\zeta = -0.56 \pm 0.50$; and solid (green) triangles: $M_w = 2.46$ kg/mol, $h_0 = 160 \pm 10$ nm, $d_0 = 630 \pm 30$ nm, $\zeta = -0.50 \pm 0.31$. (b) Least squares fit (solid line) to SC model in Eq. (1a) for 2.46 k PS with $\sigma = 0.24\ \mathrm{mC/m^2}$.

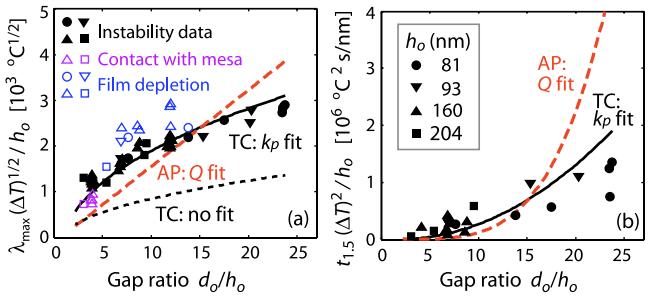

FIG. 4 (color online). (a) Comparison of measured (scaled) wavelength versus gap ratio d_0/h_0 for 2.46 kg/mol PS samples. Superimposed curves represent (i) TC model in Eq. (1c) with no fitting parameter, i.e., only the material constants given in Table I; (ii) least squares fit to AP model in Eq. (1b) with fit constant $Q = 2.3$; and (iii) least squares fit to TC model with fit constant $k_p = 0.68$ W/m K. Only data prior to contact with mesa or film depletion is included in fitting procedure. Icons shown in (b) denote initial film thickness. Error bars (not shown for clarity) extend $\pm 500\,°C^{1/2}$ along the vertical axis and ± 0.5 along the horizontal axis. Supplemental material [15] contains results for 1.3 kg/mol PS films. (b) Comparison of data in (a) with predictions of AP and TC models for growth amplitude to achieve a value $h/h_0 = 1.5$.

the TC model with fitting constant $k_p = 0.68$ W/m K, which produces excellent agreement. (The value of k_p is not expected to change significantly over the film thickness and temperature ranges used in this study [14].) Similar fits for 1.3 kg/mol PS films can be found in the supplemental section [15].

This fivefold increase in the out-of-plane thermal conductivity is suggestive of polymer chain alignment. Birefringence measurements of spun coat and annealed PS films (150 kg/mol, 2.3 μm) have established out-of-plane alignment on oxide coated wafers [16]. Additional studies have shown that the thermal conductivity of polymer microscale films can increase by a factor 4–8 in the direction of alignment [14]. Chain alignment is also observed to increase with decreasing molecular weight and decreasing film thickness [17]. Simultaneous adjustment of other material constants in Eq. (1c) was also tested, but only an increase in k_p captures the correct dependence of λ_{max}^{TC} with d_0/h_0 for the range shown.

The time for protrusions to reach a normalized height h/h_0 can also be estimated from linear stability theory [8]:

$$t_{h/h_0} = \frac{3\eta h_0}{\gamma}\left(\frac{\lambda_{max}}{2\pi h_0}\right)^4 \log\left(\frac{h/h_0 - 1}{R/h_0}\right). \quad (2)$$

Here, R/h_0 denotes the normalized initial film roughness, estimated to be 10^{-2} from atomic force microscopy. The average (scaled) value of $t_{1.5}$ is shown in Fig. 4(b) using the best fit values for λ_{max} from Fig. 4(a). Variations in film thickness were obtained from interference color mapping. As evident, the TC model for 2.46 kg/mol PS with fitting parameter $k_p = 0.68$ W/m K yields a closer fit to the experimental data than the AP model.

In summary, these experiments establish that thermocapillary forces along the free surface of the nanofilm generate a long wavelength thermocapillary instability primarily responsible for the formation and growth of nanopillar arrays. Excellent agreement with theory is obtained for a value of the melt out-of-plane thermal conductivity several times larger than bulk. This is suggestive of polymer chain alignment in the vertical direction. Studies of the degree of alignment as a function of chain length are currently underway. We are hopeful that the excellent correspondence between experiment and theory will lead to further reduction in the pitch and higher spatial resolution for fabrication of optical and photonic arrays.

This study was funded by NSF grants CTS-0649474 and CBET 0701324.

*stroian@caltech.edu

[1] S. Y. Chou, L. Zhuang, and L. Guo, Appl. Phys. Lett. **75**, 1004 (1999).
[2] L. Zhuang, Ph.D. thesis, Princeton Univ., Princeton, NJ, 2002.
[3] E. Schäffer *et al.*, Macromolecules **36**, 1645 (2003).
[4] J. Peng *et al.*, Polymer **45**, 8013 (2004).
[5] S. Y. Chou and L. Zhuang, J. Vac. Sci. Technol. B **17**, 3197 (1999).
[6] E. Schäffer *et al.*, Europhys. Lett. **60**, 255 (2002).
[7] M. Dietzel and S. M. Troian, Phys. Rev. Lett. **103**, 074501 (2009).
[8] M. Dietzel and S. M. Troian, J. Appl. Phys. **108**, 074308 (2010).
[9] M. L. Williams, J. Appl. Phys. **29**, 1395 (1958).
[10] COMSOL Multiphysics®, Inc., Los Angeles, CA.
[11] Z. Pu, in *Polymer Data Handbook*, edited by J. E. Mark (Oxford Univ. Press, NY, 1999).
[12] A. Naranjo *et al.*, *Plastics Testing and Characterization* (Hanser Gardner, Cincinnati, 2008).
[13] M. F. Al-Adel, D. A. Saville, and S. Sundaresan, Ind. Eng. Chem. Res. **41**, 6224 (2002).
[14] K. Kurabayashi *et al.*, J. Microelectromech. Syst. **8**, 180 (1999).
[15] See supplemental material at http://link.aps.org/supplemental/10.1103/PhysRevLett.106.175501.
[16] F. Ay *et al.*, J. Appl. Phys. **96**, 7147 (2004).
[17] Y. Cohen and S. Reich, J. Poly. Sci.: Poly. Phys. Edn. **19**, 599 (1981).
[18] W. Fulkerson *et al.*, Phys. Rev. **167**, 765 (1968).
[19] J. R. Welty, C. E. Wicks, and R. E. Wilson, *Fundamentals of Momentum, Heat, and Mass Transfer* (John Wiley & Sons, New York, 1984), 3rd ed.
[20] Y. S. Touloukian *et al.*, *Thermal Conductivity—Nonmetallic Solids* (Plenum, NY, 1970), Vol. 2.